molecules

MDPI

Article

In Situ Decoration of Bi_2S_3 Nanosheets on Zinc Oxide/Cellulose Acetate Composite Films for Photodegradation of Dyes under Visible Light Irradiation

Yixiao Dan [1,†], Jialiang Xu [1,†], Jian Jian [1,*], Lingxi Meng [1], Pei Deng [1], Jiaqi Yan [2,*], Zhengqiu Yuan [1], Yusheng Zhang [1] and Hu Zhou [1]

[1] Hunan Engineering Research Center for Functional Film Materials, School of Chemistry and Chemical Engineering, Hunan University of Science and Technology, Xiangtan 411201, China; dyx13536505551@gmail.com (Y.D.); isxujialiang@163.com (J.X.); lingximengqr@163.com (L.M.); dengpei0901@163.com (P.D.); yuanzhengqiu@126.com (Z.Y.); zys_2002@hotmail.com (Y.Z.); hnustchemzhou@163.com (H.Z.)

[2] Furong College, Hunan University of Arts and Science, Changde 415000, China

* Correspondence: jianjianjqr@126.com (J.J.); theyjq@outlook.com (J.Y.)

† These authors contributed equally to this work.

Abstract: A novel Bi_2S_3-zinc oxide/cellulose acetate composite film was prepared through a blending-wet phase conversion and in situ precipitate method. The results revealed that the incorporation of Bi_2S_3 in the film increased the cavity density and uniformity, which provided additional space for the growth of active species and improved the interaction between dye pollutants and active sites. Zinc oxide acted as a mediator to facilitate the separation of electron–hole pairs effectively preventing their recombination, thus reducing the photo-corrosion of Bi_2S_3. As a result, the Bi_2S_3-ZnO/CA composite film exhibited favorable photocatalytic activity in the degradation of various dyes. Additionally, the composite film displayed effortless separation and recovery without the need for centrifugation or filtration, while maintaining its exceptional catalytic performance even after undergoing various processes.

Keywords: cellulose acetate; ZnO; Bi_2S_3; photocatalytic; dye degradation

check for updates

Citation: Dan, Y.; Xu, J.; Jian, J.; Meng, L.; Deng, P.; Yan, J.; Yuan, Z.; Zhang, Y.; Zhou, H. In Situ Decoration of Bi_2S_3 Nanosheets on Zinc Oxide/Cellulose Acetate Composite Films for Photodegradation of Dyes under Visible Light Irradiation. *Molecules* **2023**, *28*, 6882. https://doi.org/10.3390/molecules28196882

Academic Editor: Sugang Meng

Received: 23 August 2023
Revised: 25 September 2023
Accepted: 26 September 2023
Published: 29 September 2023

Copyright: © 2023 by the authors. Licensee MDPI, Basel, Switzerland. This article is an open access article distributed under the terms and conditions of the Creative Commons Attribution (CC BY) license (https://creativecommons.org/licenses/by/4.0/).

1. Introduction

The advancement of the textile industry has yielded economic affluence and societal equilibrium for humanity. Nevertheless, due to its highly polluting nature, the textile industry generates approximately 1.6 million liters of dyes per day [1–3]. This substantial dye consumption has resulted in a significant volume of dye wastewater, posing severe threats to both the ecological environment and human well-being [4,5]. Consequently, individuals have implemented diverse approaches, including biological, physical, and chemical methods, to effectively and safely treat dye wastewater [6]. The efficacy of conventional treatment methods is frequently constrained by the considerable persistence and solubility of synthetic dyes in water. There is a pressing need to establish economically viable and ecologically sound treatment approaches that can effectively address dye wastewater prior to its ultimate release into the environment. Photocatalytic technology, characterized by its straightforward procedural nature, gentle operating conditions, and environmentally friendly attributes, offers a viable solution by facilitating the degradation of organic pollutants in aqueous solutions into H_2O, CO_2, or other diminutive molecules [7–9]. However, the powdered photocatalyst tends to agglomerate during the process of photocatalysis, resulting in a challenge to separating and recycling. Additionally, this agglomeration can lead to secondary pollution in the water system, thereby limiting its effectiveness in degrading organic pollutants [10–12]. Therefore, it becomes imperative to develop an

appropriate support substrate that can address these issues by facilitating the deposition of the catalyst [13].

Cellulose acetate (CA) is classified as a biopolymer, possessing notable attributes such as exceptional biocompatibility, biodegradability, robust mechanical strength, hydrophilicity, and film-forming capabilities. Consequently, it has found extensive applications in diverse sectors including medical care, packaging, textile, filtration, and various other domains [14–16]. However, the practical application of CA is impeded by its susceptibility to microbial attack, which poses a significant challenge. Despite the potential limitation of biofouling on CA films in water purification, the integration of nanotechnology and membrane loading technology presents a promising solution to overcome the drawbacks associated with cellulose acetate. Fu et al. [17] conducted a one-step coagulation process in Na_2SO_4 aqueous solutions to produce cellulose-based ZnO nanocomposite films. These films demonstrated remarkable UV-blocking properties and antibacterial activities. Similarly, Abad et al. [18] employed a phase inversion and co-precipitation method to create a CA/Au/ZnO film, which exhibited high photocatalytic activity and achieved a 95.28% degradation rate of Eosin Y pollutant. The incorporation of nanocomposite technology into fiber films can enhance their characteristics, thereby addressing their limitations and enabling their use as catalyst support substrates.

Bismuth sulfide (Bi_2S_3) is a promising candidate for contaminant removal, electrochemical energy conversion, and storage due to its electrical and optical properties [19–21]. Additionally, Bi_2S_3 possesses advantageous characteristics including an appropriate band gap (1.33 eV), strong visible light absorption capability, high carrier mobility, and nontoxicity [22]. Furthermore, Bi_2S_3 can be easily synthesized through a straightforward solution method at room temperature. However, the utilization of Bi_2S_3 as a sole photocatalyst encounters challenges due to its rapid recombination as a photogenerated electron–hole pair and photoinduced corrosion [23]. One approach to enhance the photocatalytic efficiency of Bi_2S_3 involves combining it with another photocatalytic semiconductor possessing suitable band positioning to mitigate the recombination efficiency of its photogenerated carriers. Sang et al. [24] constructed nanoflower-like Bi_2O_3/Bi_2S_3 heterojunctions that were fabricated through a one-step hydrothermal method, and obtained a removal rate of 99.72% for rhodamine B (RhB) and 91.80% for Cr(VI), respectively. Similarly, Lu et al. [25] synthesized nuclear-shell structure TiO_2/Bi_2S_3 heterojunctions using the coprecipitation method, and the results indicated that an optimal quantity of Bi_2S_3 could enhance the photocatalytic activity of TiO_2. The removal rate of methyl orange (MO) for TiO_2/Bi_2S_3 can reach 99% within 10 min under UV irradiation. Zinc oxide (ZnO) is a typical n-type semiconductor due to its wide band gap (3.37 eV) and the low cost of raw materials that have attracted people's attention in the field of ultraviolet detection [26,27]. The effective detection of UV light by a single ZnO is limited due to the rapid recombination of electron–hole pairs under illumination, which hinders its practical application [28,29]. It is possible to form a type-II band structure by matching the band positions between Bi_2S_3 and ZnO. Yuan et al. [30] successfully prepared a ZnO/Bi_2S_3 photocatalyst with a heterojunction structure using a solvothermal method for Cr(VI) removal and obtained a removal rate of 96% within 120 min under visible-light irradiation. It can be seen that the coupling of Bi_2S_3 with ZnO to form a heterostructure and stably loading it on the CA composite film present a novel and significant research idea for supported photocatalysts.

In this study, a novel stable Bi_2S_3-ZnO/CA composite film was successfully prepared by the blending-wet phase conversion and in situ synthesis method. SEM, XRD, XPS, and PL were used to characterize the morphology, phase structure, element valence, and electron–hole pair recombination ability of the prepared composite materials. The photocatalytic performance and stability of RhB as a model pollutant were evaluated in the presence of visible light. In addition, different dyes were tested under different conditions to determine the photocatalytic activity of the composite film, and the photocatalytic mechanism was speculated through the active species capture experiment.

2. Results and Discussion

2.1. Structural Characterization

The surface and internal structures of pure CA, ZnO/CA, Bi_2S_3/CA, and Bi_2S_3-ZnO/CA composite films were observed by FE-SEM characterization, and the results are shown in Figure 1. The surface images reveal a thickness of approximately 200 µm for the composite films. Figure 1(a_1–a_3) illustrate that the pure CA composite film exhibits a characteristic asymmetric structure comprising of sponge-like hollow fiber skin and irregular cavities [31,32]. Upon loading ZnO onto the CA film, as depicted in Figure 1(b_1–b_3), the surface of the composite film becomes smoother and the number of pores decreases significantly. Additionally, the rod-shaped ZnO is observed to extend from the interior to the exterior of the thin film, indicating a favorable integration between ZnO and CA [33]. As demonstrated in Figure 1(c_1–c_3), the Bi_2S_3 within the Bi_2S_3/CA composite film is observed to form a granular cluster on the film's surface. Furthermore, the incorporation of Bi_2S_3 enhances the density and uniformity of the cavities within the composite film. These cavities provide additional space for the growth of active species and enhance the contact efficiency between water pollutants and photocatalysts [34]. Figure 1(d_1–d_3) depict the notable alterations in the morphology and distribution of Bi_2S_3 within the Bi_2S_3-ZnO/CA composite film in the presence of ZnO. The incorporation of ZnO into the composite film leads to a notable improvement in surface smoothness and a significant reduction in pore density. Consequently, the ingress of S^{2-} ions generated by thioacetamide into the pores is impeded, resulting in a lower concentration of S^{2-} ions within the ZnO/CA composite compared to the pure CA film. The elevated concentration of S^{2-} ions would promote the formation of numerous crystal nuclei and facilitate rapid crystal growth, thereby favoring the aggregation of Bi_2S_3 into granular clusters under high S^{2-} ion concentrations. Conversely, Bi_2S_3 would gradually grow at low S^{2-} ion concentrations, giving rise to the formation of flaky Bi_2S_3 nanosheets. Similar results have been verified in the relevant literature [35,36]. Therefore, the Bi_2S_3-ZnO/CA composite film displays uniform Bi_2S_3 micro-nano flakes (thickness of 10 nm and width of approximately 70 nm) and is evenly distributed within the fibers of the composite film. The EDS map of the Bi_2S_3/ZnO-CA composite film, depicted in Figure 1(e_1–e_6), illustrates a homogeneous distribution of Zn, O, Bi, and S elements throughout the composite film. This finding further confirms the attachment of nanostructured Bi_2S_3 and ZnO to the internal surface of the composite film.

The composition and crystal structure of ZnO/CA and Bi_2S_3-ZnO/CA composite films were determined by XRD characterization. As shown in Figure 2, the strong diffraction peaks appearing at 31.77°, 34.42°, 36.25°, 47.54°, 56.60°, 62.86°, 67.96°, and 69.01° in the ZnO/CA composite film corresponded to the (100), (002), (101), (102), (110), (103), (112), and (201) crystal planes, respectively. These characteristic peaks corresponded to the body-centered cubic structure of ZnO (JCPDS No. 36-1451) [37]. The addition of Bi_2S_3 resulted in a weakening of the intensity of the ZnO diffraction peaks, particularly as the Bi_2S_3 load increased. The Bi_2S_3-containing composites have quite broad diffraction peaks; this may be due to the incorporation of Bi_2S_3 in the film which increased the cavity density and uniformity, resulting in the ZnO and Bi_2S_3 being evenly distributed inside the film. Especially Bi_2S_3 coated the surface of ZnO, leading to a reduction in the diffraction peak intensity of ZnO. Furthermore, extremely weak diffraction peaks at 24.93° were observed, which corresponded to the (130) crystal planes of Bi_2S_3 [38]. The fact that the diffraction peak of Bi_2S_3 was very weak might be due to the high distribution and small size of Bi_2S_3 particles, which was consistent with findings reported in the literature [39]. These results confirmed the successful synthesis of ZnO and Bi_2S_3 in CA composite film using the in situ precipitate method.

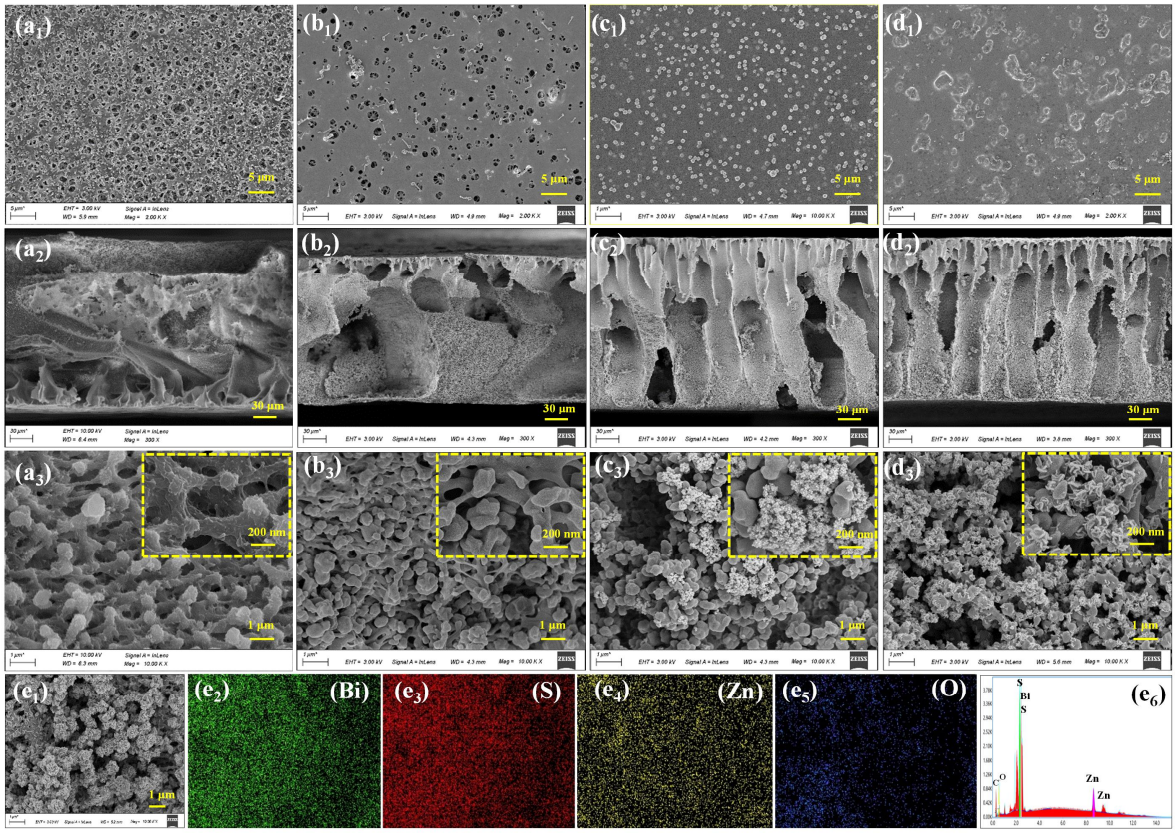

Figure 1. Surface and cross-sectional SEM images of CA (**a1**–**a3**), ZnO/CA (**b1**–**b3**), Bi_2S_3/CA (**c1**–**c3**), and Bi_2S_3-ZnO/CA (**d1**–**d3**) composite films, and EDS images of Bi_2S_3-ZnO/CA (**e1**–**e6**).

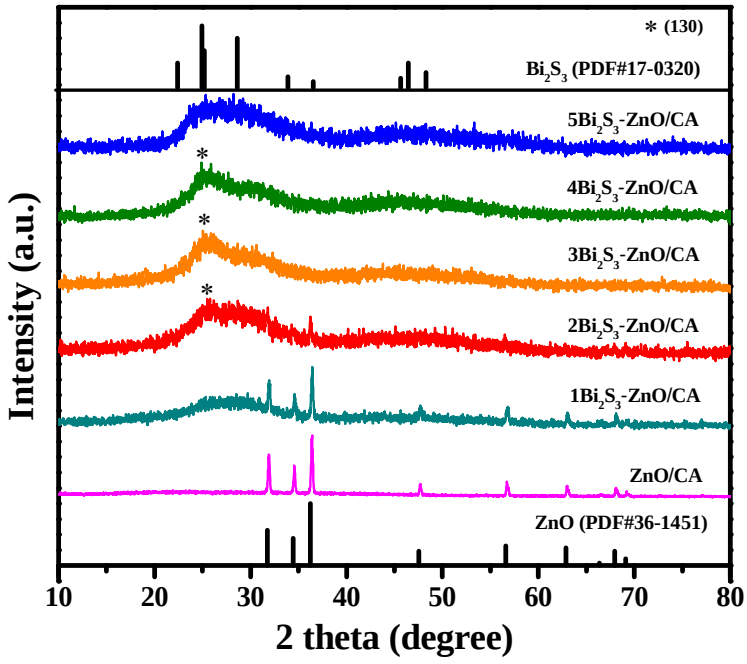

Figure 2. Typical XRD patterns of ZnO/CA and Bi_2S_3-ZnO/CA films.

Figure 3 displays the spectra of the pure CA, ZnO/CA, and Bi_2S_3-ZnO/CA composite films. The ZnO/CA spectrum exhibits characteristic peaks at 1747 cm^{-1}, 1237 cm^{-1}, 1371 cm^{-1}, and 1044 cm^{-1}, which correspond to N-H stretching vibration, C-H stretching vibration, -CH_2 symmetric stretching vibration, and free C=O stretching vibration and

partial H-bonded carbonyl stretching vibration, respectively [40,41]. The absorption peak at 482 cm^{-1} is attributed to ZnO, while the peak at 3442 cm^{-1} is associated with the O-H stretching mode [42,43]. The FTIR spectra of the pure CA film exhibit a marked resemblance to those of the Bi_2S_3-ZnO/CA and the ZnO/CA composite film, suggesting that the incorporation of bismuth sulfide and zinc oxide does not result in the formation of novel bonds with the CA film, nor does it compromise the integrity of the film's structure.

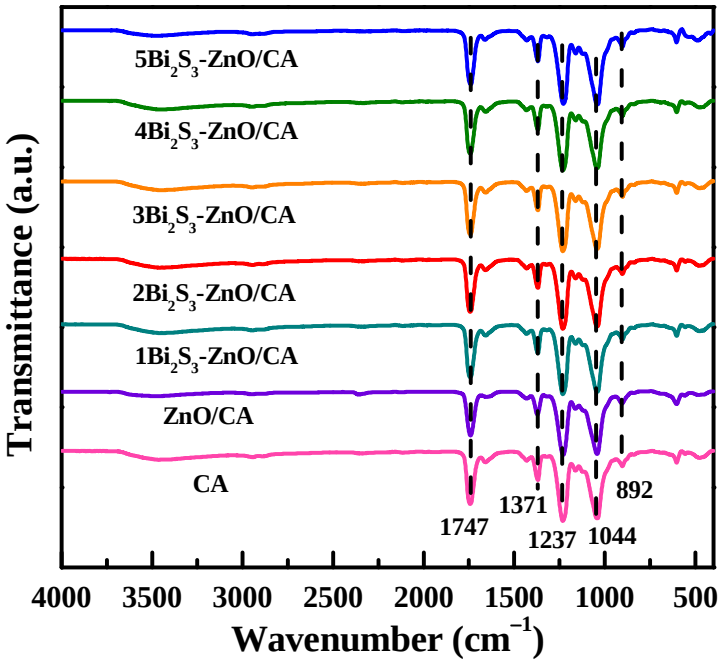

Figure 3. FTIR spectra of ZnO/CA and Bi_2S_3-ZnO/CA composite films.

The utilization of XPS spectroscopy facilitated the examination of the surface composition and chemical state of the Bi_2S_3-ZnO/CA sample, as depicted in Figure 4. The composite material is shown to contain Zn, Bi, S, O, and C elements, as demonstrated by the comprehensive spectrum presented in Figure 4a. Figure 4b displays two prominent peaks that are concentrated at 1043.65 and 1020.28 eV, with a binding energy difference of 23.37 eV, which corresponds to Zn $2p_{1/2}$ and Zn $2p_{3/2}$, respectively. These values align with the established reference values for ZnO [44]. In Figure 4c, the high-resolution X-ray photoelectron spectroscopy spectrum of oxygen is analyzed and fitted with two distinct peaks. The weaker peak observed at 530.98 eV is attributed to the solid-state lattice oxygen present in ZnO, while the stronger peak at 531.58 eV is assigned to the interaction between carbonyl oxygen atoms in CA [37]. The Bi $4f_{7/2}$ and Bi $4f_{5/2}$ orbitals corresponding to Bi^{3+} are also observed at 156.78 eV and 162.17 eV, respectively [29]. The XPS peak of sulfur observed in Figure 4e at 162.47 eV is consistent with the standard S 2p peak, providing evidence for the formation of Bi_2S_3. In Figure 4f, the spectra associated with C can be effectively modeled with four distinct peaks at 283.58 eV, 285.07 eV, 286.12 eV, and 287.59 eV, respectively, which correspond to $H_3C(C=O)$, C-H, C-OH, and C-C-O in the CA structure [45,46]. These results not only confirm the successful synthesis of Bi2S3 but also suggest no alterations have occurred in ZnO. Additionally, the absence of any other impurities on the surface of the composite film indicates the relatively high purity of the synthesized Bi_2S_3 nanosheets.

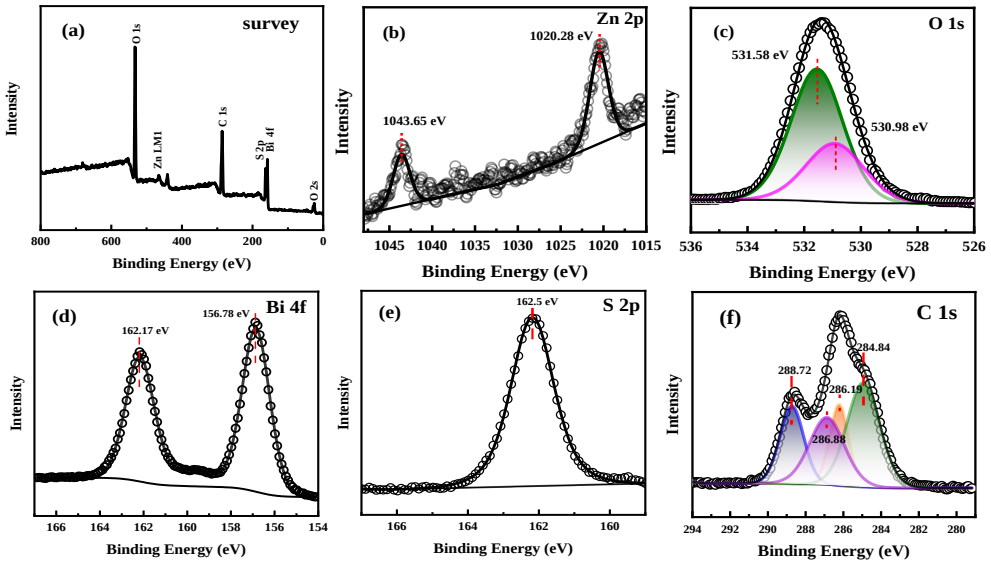

Figure 4. XPS spectra of 4Bi_2S_3-ZnO/CA composite: (**a**) survey, (**b**) Zn 2p, (**c**) O 1s, (**d**) Bi 4f, (**e**) S 2p, and (**f**) C 1s.

The optical properties of these composite films were investigated by UV-vis DRS. As illustrated in Figure 5a, both ZnO and Bi_2S_3 sensitization considerably broadened the spectrum of light absorption [47]. Notably, the Bi_2S_3 film with co-modification of ZnO and Bi_2S_3 exhibited superior visible light harvesting capabilities compared to the single Bi_2S_3 deposition, potentially due to the modulation of the bandgap by the sensitizer. The band gap width of Bi_2S_3-ZnO/CA composite film was calculated by the Tauc formula $(ahv = A(hv - E_g)^n$, where α, hv, A, and E_g were defined as the absorption coefficient, photonic energy, constant, and band gap, respectively. The n value was 1 because ZnO and Bi_2S_3 belong to direct bandgap semiconductors [48]. In Figure 5b, the calculated bandgap widths for ZnO/CA and Bi_2S_3/CA were 3.17 eV and 1.78 eV, respectively [49,50]. Additionally, the valence band (VB) and conduction band (CB) edge potentials of the ZnO/CA and Bi_2S_3/CA composite films were calculated using the empirical equations $E_{VB} = X - E_e + 0.5E_g$ and $E_{CB} = E_{VB} - E_g$. Here, E_{VB} and E_{CB} are the VB and CB edge potentials, respectively. E_e is the energy of the free electron versus hydrogen (4.5 eV), and E_g is the bandgap width. The X was the Mulliken electronegativity of the ZnO and Bi_2S_3 semiconductors, and was selected as 5.75 eV and 5.27 eV, respectively, according to the literature [49,50]. Therefore, the E_{VB} and E_{CB} values were approximately 2.84 eV and −0.34 eV (vs. NHE) for the ZnO/CA film, and 1.66 eV and −0.12 eV (vs. NHE) for the Bi_2S_3/CA film.

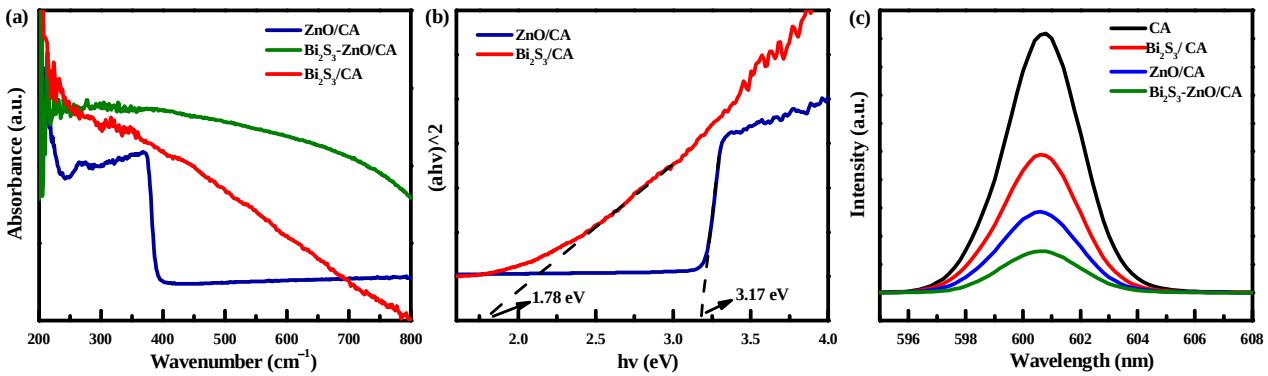

Figure 5. UV-vis DRS spectra (**a**,**b**) and PL spectra (**c**) of CA, CA/Bi_2S_3, ZnO/CA, and Bi_2S_3-ZnO/CA composite films.

Photoluminescence spectroscopy (PL) was also utilized to examine the efficacy of electron–hole pair recombination and separation in composite films. Generally, greater fluorescence intensity denotes accelerated electron–hole pair recombination rates, whereas lower fluorescence intensity signifies heightened separation efficiency [51]. Elevated electron recombination rates are disadvantageous for photocatalytic reactions. The photoluminescence spectra of pure CA, ZnO/CA, Bi_2S_3/CA, and Bi_2S_3-ZnO/CA composite films are presented in Figure 5c. ZnO/CA and Bi_2S_3/CA films exhibit an absorption peak at approximately 601 nm, while Bi_2S_3-ZnO/CA displays a lower resolution exciton absorption peak. The results suggest that the combination of ZnO and Bi_2S_3 mitigates the recombination of photo-induced electron–hole pairs and enhances the efficiency of charge separation, thereby augmenting the photocatalytic activity of the catalyst.

2.2. Photocatalytic Efficiency

The photocatalytic performance of Bi_2S_3-ZnO/CA composite films was evaluated through the degradation of RhB as a model pollutant, as depicted in Figure 6a. The absence of a photocatalyst and the sole use of a pure CA film resulted in a negligible degradation of RhB, indicating that the self-degradation effect of RhB and the adsorption effect of the CA film can be disregarded. The degradation rate of single-component ZnO/CA composite film was 26.51%, which might be attributed to the good hydrophilicity of ZnO improving the adsorption capacity of RhB. The single-component $4Bi_2S_3$/CA composite film exhibited a higher degradation rate of 50.26%, indicating that Bi_2S_3 has a favorable photocatalytic activity for RhB. The addition of ZnO and Bi_2S_3 to the CA composite film can significantly improve the photocatalytic performance, and the catalytic performance is gradually increased with the increase in the Bi_2S_3 loading. The highest degradation rate of 90.2% was achieved with the $4Bi_2S_3$-ZnO/CA film as the catalyst. Notably, a further increase in Bi_2S_3 loading led to a decline in photocatalytic efficiency. The possible reason might be that the particle aggregation at high loading resulted in a reduction in the effective active species on the composite film and a subsequent decrease in photocatalytic performance. In the Bi_2S_3-ZnO/CA catalyst, Bi_2S_3 is deemed as the primary active constituent due to its superior photocatalytic activity compared to ZnO/CA. However, ZnO acts as a mediator to facilitate the separation of electron–hole pairs, effectively preventing their recombination, thus reducing the photo-corrosion of Bi_2S_3. Consequently, this mechanism significantly enhances the overall photocatalytic efficiency.

To further investigate the degradation kinetics of RhB, a pseudo-first-order kinetic model has been employed for exploration, as illustrated in Equation (3.2): $\ln(C_0/C) = kt$ (3.2). In this equation, C_0 and C denote the initial concentration and real-time concentration of RhB, respectively, while k represents the apparent reaction rate constant under irradiation. The results of the fitting indicated that it conformed to a quasi-first-order kinetic equation. The kinetic curves of ZnO/CA, $4Bi_2S_3$/CA, and Bi_2S_3-ZnO/CA composite films are presented in Figure 6b. The apparent reaction rate constant of the $4Bi_2S_3$-ZnO/CA composite film was determined to be 0.0175 min^{-1}, which exhibited 8.8 and 4.7 times higher values compared to the single-phase ZnO/CA (0.00198min^{-1}) and $4Bi_2S_3$/CA (0.00372 min^{-1}) films, respectively. These results suggested that the synergistic effect of ZnO and Bi_2S_3 could significantly augment the photocatalytic efficiency of the composite film. Figure 6c depicts the dynamic absorbance spectra of the RhB solution on the $4Bi_2S_3$-ZnO/CA composite film under visible light irradiation. The absorbance at the maximum absorption wavelength (553 nm) of the RhB solution was gradually diminished over time and reached a negligible level after 120 min, indicating the degradation of RhB in the solution without any production of other derivatives during the photocatalysis process. Figure 6d displays the durability of the Bi_2S_3-ZnO/CA composite film in the photodegradation of RhB. The results indicated that the Bi_2S_3-ZnO/CA composite film exhibited excellent performance stability, as evidenced by the sustained degradation rate of RhB at 88% over five cycles. Additionally, the composite film can be retrieved from the aqueous phase without the requirement of centrifugal filtration, thereby preventing the loss of nanoparticles and minimizing the

risk of secondary pollution, which is advantageous for the practical implementation of photocatalysis technology.

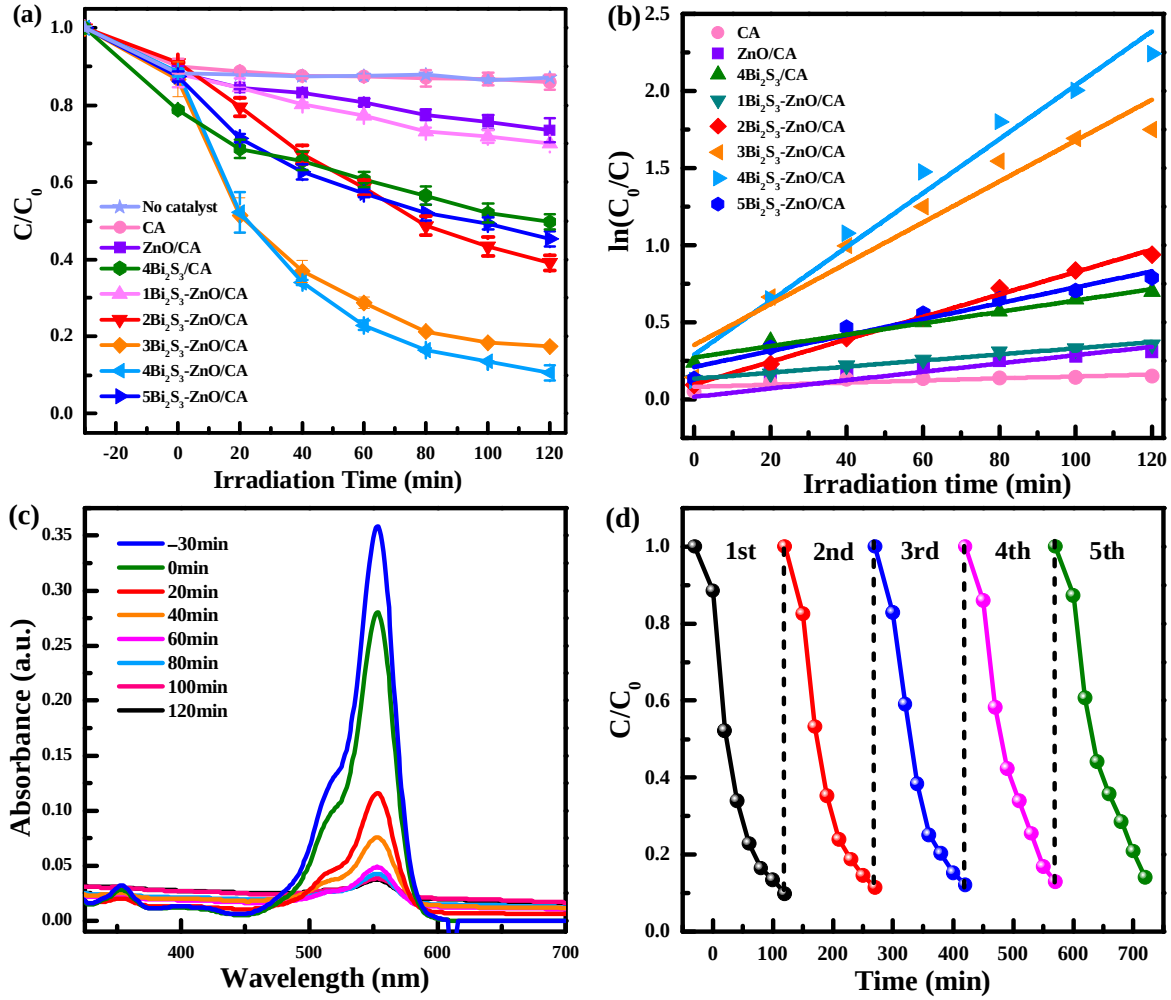

Figure 6. Photocatalytic performance of CA, ZnO/CA, Bi_2S_3/CA, and Bi_2S_3-ZnO/CA composite films with different Bi_2S_3 loading for the degradation of RhB under visible light irradiation (**a**); related degradation rate ($In(C_0/C) = kt$) plots (**b**); absorption spectrum of RhB solution in the presence of $4Bi_2S_3$-ZnO/CA composite film (**c**); and cycle runs over $4Bi_2S_3$-ZnO/CA degradation of RhB under visible light irradiation (**d**).

Figure 7a illustrates the degradation rate of RhB by a Bi_2S_3-ZnO/CA composite film under visible light conditions and varying pH levels. The photocatalytic removal rates for RhB were determined to be 91.98%, 90.16%, and 90.35% in acidic, neutral, and alkaline solutions, respectively, which suggested that the Bi_2S_3-ZnO/CA composite film exhibited commendable photocatalytic performance for RhB degradation across a broad pH range. The photodegradation of various dyes in the Bi_2S_3-ZnO/CA composite film was also investigated and the results are presented in Figure 7b. The removal rates of RhB, malachite green (MG), methylene blue (MB), and crystal violet (CV) were 90.16%, 88.85%, 86.88%, and 87.20%, respectively. These results suggested that the Bi_2S_3-ZnO/CA composite film exhibited a universal capacity for dye pollutant treatment. Furthermore, the aforementioned dyes demonstrated commendable photocatalytic efficacy in the presence of natural light (the sunlight between 2:00 p.m. and 4:00 p.m. on a sunny day with a PM 2.5 of 26 micrograms per cubic meter in Xiangtan, Hunan, China). The solar insolation was measured and recorded by an optical power meter. Notably, RhB and CV exhibited a degradation efficiency reduction of merely 2% and 4% in comparison to simulating visible

light. In addition, the photocatalytic activity of the Bi_2S_3-ZnO/CA composite film is slightly lower than that reported in other related studies (Table 1). This may be due to the better mass transfer effect of the powder compared to the film. However, composite film materials have better practical application prospects because of their easy separation and recovery in dye wastewater treatment.

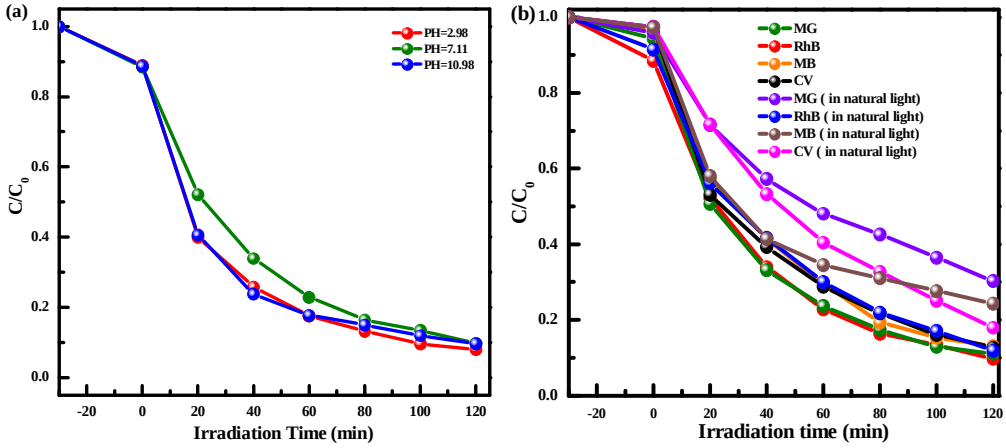

Figure 7. Effect of pH for the photodegradation of RhB on the $4Bi_2S_3$-ZnO/CA composite film (**a**); degradation of different dyes by the $4Bi_2S_3$-ZnO/CA composite film under a xenon lamp and natural light conditions (**b**).

Table 1. Performance of different Bi_2S_3-based composites for the photodegradation of dyes under visible light.

Photocatalyst	Photocatalyst Form	Catalyst Dosage /(g/L)	Dye Concentration /(mg/L)	Time /min	pH Levels	Degradation Rate/min	Ref.
Bi_2S_3-BiOI	powder	1.0	10.0-RhB	60	8–9	>99.0	[21]
SnO_2/Bi_2S_3-Bi25	powder	0.33	10.0-RhB	180	8–9	>80.0	[23]
Bi_2O_3-Bi_2S_3	powder	0.5	20.0-RhB	90	8–9	>99.0	[24]
TiO_2-Bi_2S_3	powder	5.0	20.0-MO	10	3–4	>99.0	[25]
Bi_2S_3-BiOBr/TiO_2 NTA	powder	0.05	20.0-RhB	180	8–9	>98.0	[35]
Bi_2S_3-ZnO/CA	film	1.0	10.0-RhB	120	3–11	>90.0	This work

To ascertain the photocatalytic degradation mechanism, radical-trapping experiments were conducted utilizing isopropanol (IPA), triethanolamine (TEOA), and 4-hydroxy-TEMPO (TEMPO) as scavengers for hydroxyl groups (•OH), holes (h^+), and superoxide radicals ($\bullet O_2^-$), respectively [52,53]. Figure 8 demonstrates that the inclusion of IPA had negligible impact on the degradation of RhB, thereby suggesting that •OH played a minor role in the photodegradation of RhB by the Bi_2S_3-ZnO/CA composite film. Conversely, the presence of TEOA and TEMPO resulted in a substantial inhibition of the RhB degradation, indicating that h^+ and $\bullet O_2^-$ were the primary active components responsible for the photocatalytic degradation of RhB by the Bi_2S_3-ZnO/CA composite film.

Based on the aforementioned results, the potential mechanism for the photodegradation of RhB by the Bi_2S_3/ZnO-CA composite film was hypothesized, as illustrated in Scheme 1. When exposed to visible light, both the ZnO and Bi_2S_3 particles present in the film were stimulated to generate electrons and holes in their respective conduction and valence bands. Due to the more negative conduction band (CB) energy of ZnO (−0.34 eV/NHE) compared to that of Bi_2S_3 (−0.12 eV/NHE), the photogenerated electrons in ZnO readily migrated to the CB of Bi_2S_3, where they were scavenged by the available

surface O_2 to produce $\bullet O_2^-$ radicals [54]. Simultaneously, the photogenerated holes in ZnO migrated to the valence band (VB) of Bi_2S_3 due to the higher VB energy of ZnO (+2.84 eV/NHE) compared to Bi_2S_3 (+1.66 eV/NHE). The abundant concentration of reactive holes in the Bi_2S_3 VB effectively oxidizes the dye [55]. The strong oxidation ability of these holes and $\bullet O_2^-$ radicals can over-decompose RhB into harmless molecules such as CO_2 and H_2O. As a result, the separation of electron–hole pairs is efficiently achieved, leading to a significant reduction in charge recombination and an enhancement in the photocatalytic activity of the composite film.

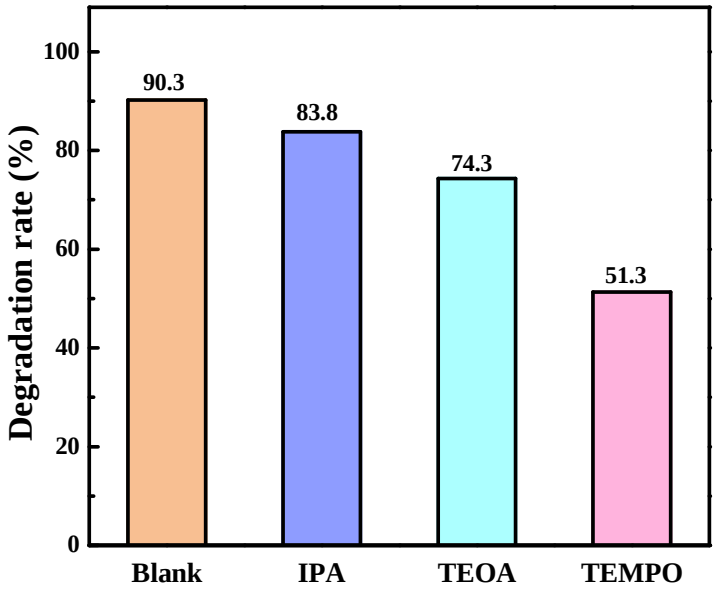

Figure 8. Trapping experiment of the active species over the Bi_2S_3-ZnO/CA composite film for RhB degradation.

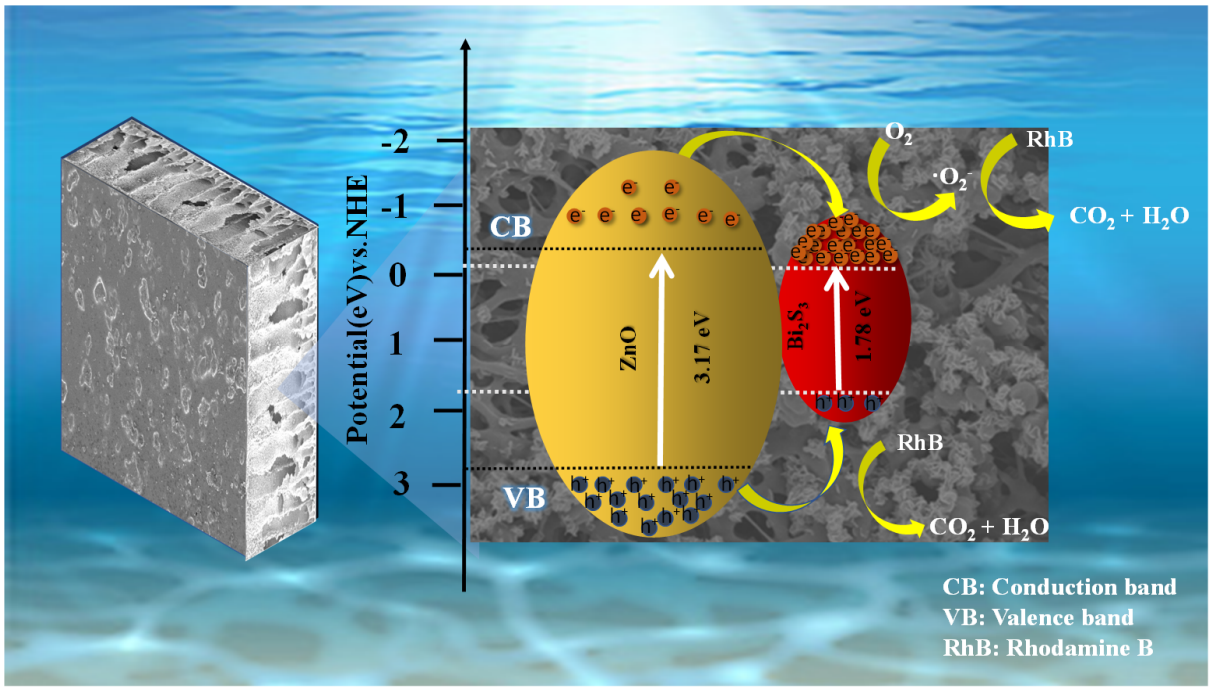

Scheme 1. Catalytic mechanism of RhB degradation by Bi_2S_3-ZnO/CA composite film.

3. Experimental Section

3.1. Synthesis of Bi_2S_3-ZnO/CA Composite Films

The Bi_2S_3-ZnO/CA composite films were prepared by blending-wet phase conversion and in situ precipitate method [53,56]; the detailed steps are presented in Scheme 2. Typically, 2 g CA, 1 g ZnO, and $Bi(NO_3)_3 \bullet 5H_2O$ at different quantities (1, 2, 3, 4, and 5 g) were successively added to the 20 g DMF solvent with vigorous stirring at room temperature for 2 h. The obtained uniformly mixed solution was held in the air for 30 min to eliminate bubbles. Subsequently, the mixture was cast evenly on the glass mold, and quickly immersed in thioacetamide solutions (equimolar with $Bi(NO_3)_3 \bullet 5H_2O$) for 8 h to the in situ synthesis of Bi_2S_3-ZnO/CA composite films [35]. Afterward, the resultant composite films were rinsed with ethanol and deionized water several times, and subsequently dried overnight at −40 °C in a freeze-drying oven. Based on the content of $Bi(NO_3)_3 \bullet 5H_2O$, the acquired films were labeled as $1Bi_2S_3$-ZnO/CA, $2Bi_2S_3$-ZnO/CA, $3Bi_2S_3$-ZnO/CA, $4Bi_2S_3$-ZnO/CA, and $5Bi_2S_3$-ZnO/CA, respectively. By comparison, the pure CA, ZnO/CA, and Bi_2S_3/CA films were also prepared using the same methods.

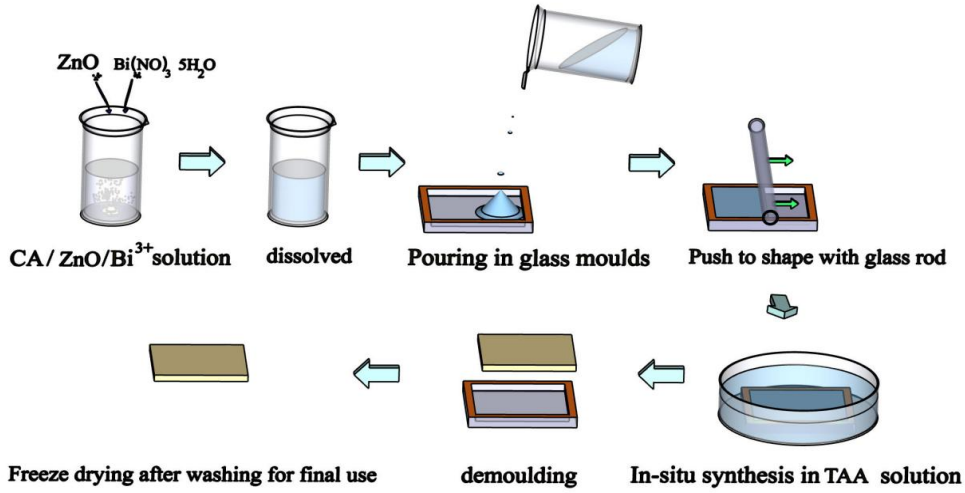

Scheme 2. The preparation process for the synthesis of Bi_2S_3-ZnO/CA composite films.

3.2. Characterization

The crystal structures of the composite films were analyzed using the X-ray diffraction (XRD) measurement on a Brucker AXS D8-Advance with Cu-Kα irradiation. The morphology of the samples was observed by Field Emission Scanning Electron Microscopy (FE-SEM, Zeiss Sigma 300). FT-IR spectra were recorded using a Brucker TENSORII FT-IR spectrometer from 4000 to 400 cm^{-1}. Surface electronic states were detected using X-ray photoelectron spectroscopy (XPS) using a K-Alpha 1063, and all binding energies were corrected by a C1s peak at 284.8 eV. The composite films' UV-vis diffuse reflectance spectra (DRS) were obtained using a Shimadzu UV-2550 spectrophotometer. The recombination of electron–hole pairs was explored using photoluminescence spectroscopy (PL) on HitachiF-2700.

3.3. Evaluation of Photocatalytic Activity

The photocatalytic activities of composite films were evaluated by the degradation of dyes under visible light illumination using a 300W Xe lamp equipped with a UV cutoff filter (λ between 420 and 800 nm). Generally, 0.2 g of catalyst was added to a condensation reactor containing 200 mL of RhB (10 mg/L). The suspension was continuously stirred for 30 min in the dark to achieve an adsorption–desorption equilibrium between the composite film and RhB-simulated liquid. Then, the mixture was subjected to photocatalysis using a xenon-mercury parallel light source. During the photocatalytic reaction, 10 mL of the reaction solution was sampled every 20 min. The residual concentration of RhB was

measured using a UV-visible spectrophotometer at the maximum absorption wavelength. In addition, hydroxyl (•OH), holes (h^+), and superoxide radicals ($\bullet O_2^-$) were detected with IPA, TEOA, and TEMPO in this photocatalytic reaction, respectively.

4. Conclusions

In summary, a novel Bi_2S_3/ZnO-CA composite film was successfully prepared through the blending-wet phase conversion and in situ precipitate techniques. The results indicated that the incorporation of ZnO induced a notable modification in the configuration and dispersion of Bi_2S_3 particles, transitioning from clustered nanospheres to evenly distributed nanosheets. Furthermore, ZnO acted as a mediator for the separation of electron–hole pairs, effectively impeding the recombination of photo-generated electron–hole pairs and mitigating the photo-corrosion of sulfides. Among the catalysts, the $4Bi_2S_3$/ZnO-CA composite film showed the best photocatalytic activity with a 90.16% RhB degradation rate. More importantly, the composite film presented advantages in terms of operational simplicity, facile recovery, and the elimination of secondary pollution compared to powder-type photocatalysts, rendering it an efficient and versatile material for wastewater treatment.

Author Contributions: Y.D.: writing—original draft preparation and software. J.X.: investigation and formal analysis. J.J.: writing—review and editing, funding acquisition, and resources. L.M.: data curation. P.D.: methodology. J.Y.: conceptualization and supervision. Z.Y.: visualization. Y.Z.: validation. H.Z.: project administration. All authors have read and agreed to the published version of the manuscript.

Funding: This work was funded by the National Natural Science Foundation of China (22202068), the Natural Science Foundation in Hunan Province (2021JJ30239), and the Natural Science Foundation for Distinguished Young Scholars in Hunan Province (2020JJ2014).

Institutional Review Board Statement: Not applicable.

Informed Consent Statement: Not applicable.

Data Availability Statement: The data in this study are available from the corresponding author upon reasonable request.

Conflicts of Interest: The authors declare that they have no known competing financial interests or personal relationships that could have appeared to influence the work reported in this paper.

Sample Availability: Samples of some compounds may be available from the authors.

References

1. Uddin, F. Environmental hazard in textile dyeing wastewater from local textile industry. *Cellulose* **2021**, *28*, 10715–10739. [CrossRef]
2. Zhang, L.; Meng, Y.; Xie, B.; Ni, Z.; Xia, S. Br doping promotes the transform of Cu_2O (100) to Cu_2O (111) and facilitates efficient photocatalytic degradation of tetracycline. *Mol. Catal.* **2023**, *548*, 113431. [CrossRef]
3. Zhang, L.; Chen, L.; Xia, Y.; Liang, Z.; Huang, R.; Liang, R.; Yan, G. Modification of polymeric carbon nitride with Au–CeO_2 hybrids to improve photocatalytic activity for hydrogen evolution. *Molecules* **2022**, *27*, 7489. [CrossRef] [PubMed]
4. Kesraoui, A.; Selmi, T.; Seffen, M.; Brouers, F. Influence of alternating current on the adsorption of indigo carmine. *Environ. Sci. Pollut. Res.* **2017**, *24*, 9940–9950. [CrossRef]
5. Sarma, G.K.; Gupta, S.S.; Bhattacharyya, K.G. RETRACTED: Adsorption of Crystal violet on raw and acid-treated montmorillonite, K10, in aqueous suspension. *J. Environ. Manag.* **2016**, *171*, 1–10. [CrossRef]
6. Barisci, S.; Inan, H.; Turkay, O.; Dimoglo, A.; Erol, D. Degradation of toxic indigo carmine dye by electrosynthesized ferrate (VI). *J. Appl. Solut. Chem. Model.* **2017**, *6*, 75–83. [CrossRef]
7. Ibrahim, Y.O.; Gondal, M. Visible-light-driven photocatalytic performance of a Z-scheme based TiO_2/WO_3/g-C_3N_4 ternary heterojunctions. *Mol. Catal.* **2021**, *505*, 111494. [CrossRef]
8. Gupta, V.K.; Jain, R.; Mittal, A.; Saleh, T.A.; Nayak, A.; Agarwal, S.; Sikarwar, S. Photo-catalytic degradation of toxic dye amaranth on TiO_2/UV in aqueous suspensions. *Mater. Sci. Eng. C* **2012**, *32*, 12–17. [CrossRef]
9. Yu, Z.; Qian, L.; Zhong, T.; Ran, Q.; Huang, J.; Hou, Y.; Li, F.; Li, M.; Sun, Q.; Zhang, H. Enhanced visible light photocatalytic activity of CdS through controllable self-assembly compositing with ZIF-67. *Mol. Catal.* **2020**, *485*, 110797. [CrossRef]
10. Wu, G.; Liang, R.; Ge, M.; Sun, G.; Zhang, Y.; Xing, G. Surface passivation using 2D perovskites toward efficient and stable perovskite solar cells. *Adv. Mater.* **2022**, *34*, 2105635. [CrossRef]

11. Ge, M.; Cao, C.; Huang, J.; Li, S.; Chen, Z.; Zhang, K.-Q.; Al-Deyab, S.; Lai, Y. A review of one-dimensional TiO_2 nanostructured materials for environmental and energy applications. *J. Mater. Chem. A* **2016**, *4*, 6772–6801. [CrossRef]
12. Wang, Y.; Liu, Z.; Li, Y.; Yang, X.; Zhao, L.; Peng, J. Boosting Photocatalytic Performance of ZnO Nanowires via Building Heterojunction with g-C_3N_4. *Molecules* **2023**, *28*, 5563. [CrossRef] [PubMed]
13. Zhang, S.; Yan, Y.; Hu, W.; Fan, Y. Mesoporous CuO Prepared in a Natural Deep Eutectic Solvent Medium for Effective Photodegradation of Rhodamine B. *Molecules* **2023**, *28*, 5554. [CrossRef] [PubMed]
14. Jatoi, A.W.; Khatri, Z.; Ahmed, F.; Memon, M.H. Effect of silicone nano, nano/micro and nano/macro-emulsion softeners on color yield and physical characteristics of dyed cotton fabric. *J. Surfactants Deterg.* **2015**, *18*, 205–211. [CrossRef]
15. Wang, X.; Zhao, Y.; Li, F.; Dou, L.; Li, Y.; Zhao, J.; Hao, Y. A chelation strategy for in-situ constructing surface oxygen vacancy on {001} facets exposed BiOBr nanosheets. *Sci. Rep.* **2016**, *6*, 24918. [CrossRef]
16. Wang, M.; Ge, R.; Zhao, P.; Williams, G.R.; Yu, D.; Bligh, S.A. Exploring wettability difference-driven wetting by utilizing electrospun chimeric Janus microfiber comprising cellulose acetate and polyvinylpyrrolidone. *Mater. Des.* **2023**, *226*, 111652. [CrossRef]
17. Fu, F.; Li, L.; Liu, L.; Cai, J.; Zhang, Y.; Zhou, J.; Zhang, L. Construction of cellulose based ZnO nanocomposite films with antibacterial properties through one-step coagulation. *ACS Appl. Mater. Interfaces* **2015**, *7*, 2597–2606. [CrossRef]
18. Abad, S.N.K.; Mozammel, M.; Moghaddam, J.; Mostafaei, A.; Chmielus, M. Highly porous, flexible and robust cellulose acetate/Au/ZnO as a hybrid photocatalyst. *Appl. Surf. Sci.* **2020**, *526*, 146237. [CrossRef]
19. Mahapatra, A.D.; Basak, D. Enhanced ultraviolet photosensing properties in Bi_2S_3 nanoparticles decorated ZnO nanorods' heterostructure. *J. Alloys Compd.* **2019**, *797*, 766–774. [CrossRef]
20. Luo, W.; Li, F.; Li, Q.; Wang, X.; Yang, W.; Zhou, L.; Mai, L. Heterostructured Bi_2S_3-Bi_2O_3 nanosheets with a built-in electric field for improved sodium storage. *ACS Appl. Mater. Interfaces* **2018**, *10*, 7201–7207. [CrossRef]
21. Ju, P.; Zhang, Y.; Hao, L.; Cao, J.; Zhai, X.; Dou, K.; Jiang, F.; Sun, C. 1D Bi_2S_3 nanorods modified 2D BiOI nanoplates for highly efficient photocatalytic activity: Pivotal roles of oxygen vacancies and Z-scheme heterojunction. *J. Mater. Sci. Technol.* **2023**, *142*, 45–59. [CrossRef]
22. Huang, W.; Xing, C.; Wang, Y.; Li, Z.; Wu, L.; Ma, D.; Dai, X.; Xiang, Y.; Li, J.; Fan, D. Facile fabrication and characterization of two-dimensional bismuth (III) sulfide nanosheets for high-performance photodetector applications under ambient conditions. *Nanoscale* **2018**, *10*, 2404–2412. [CrossRef]
23. Fenelon, E.; Bui, D.; Tran, H.H.; You, S.; Wang, Y.; Cao, T.; Van Pham, V. Straightforward synthesis of SnO_2/Bi_2S_3/BiOCl-$Bi_{24}O_{31}C_{l10}$ composites for drastically enhancing rhodamine B photocatalytic degradation under visible light. *ACS Omega* **2020**, *5*, 20438–20449. [CrossRef] [PubMed]
24. Sang, Y.; Cao, X.; Dai, G.; Wang, L.; Peng, Y.; Geng, B. Facile one-pot synthesis of novel hierarchical Bi_2O_3/Bi_2S_3 nanoflower photocatalyst with intrinsic pn junction for efficient photocatalytic removals of RhB and Cr (VI). *J. Hazard. Mater.* **2020**, *381*, 120942. [CrossRef]
25. Lu, J.; Han, Q.; Wang, Z. Synthesis of TiO_2/Bi_2S_3 heterojunction with a nuclear-shell structure and its high photocatalytic activity. *Mater. Res. Bull.* **2012**, *47*, 1621–1624. [CrossRef]
26. Ouyang, W.; Teng, F.; Jiang, M.; Fang, X. ZnO film UV photodetector with enhanced performance: Heterojunction with $CdMoO_4$ microplates and the hot electron injection effect of Au nanoparticles. *Small* **2017**, *13*, 1702177. [CrossRef]
27. Tian, C.; Zhang, Q.; Wu, A.; Jiang, M.; Liang, Z.; Jiang, B.; Fu, H. Cost-effective large-scale synthesis of ZnO photocatalyst with excellent performance for dye photodegradation. *Chem. Commun.* **2012**, *48*, 2858–2860. [CrossRef]
28. Bai, Z.; Fu, M.; Zhang, Y. Vertically aligned and ordered ZnO/CdS nanowire arrays for self-powered UV-visible photosensing. *J. Mater. Sci.* **2017**, *52*, 1308–1317. [CrossRef]
29. Yi, S.; Zhao, F.; Yue, X.; Wang, D.; Lin, Y. Enhanced solar light-driven photocatalytic activity of BiOBr-ZnO heterojunctions with effective separation and transfer properties of photo-generated chargers. *New J. Chem.* **2015**, *39*, 6659–6666. [CrossRef]
30. Yuan, X.; Wu, X.; Feng, Z.; Jia, W.; Zheng, X.; Li, C. Facile synthesis of heterojunctioned ZnO/Bi_2S_3 nanocomposites for enhanced photocatalytic reduction of aqueous Cr (VI) under visible-light irradiation. *Catalysts* **2019**, *9*, 624. [CrossRef]
31. Zhou, Z.; Peng, X.; Zhong, L.; Wu, L.; Cao, X.; Sun, R.C. Electrospun cellulose acetate supported Ag@AgCl composites with facet-dependent photocatalytic properties on degradation of organic dyes under visible-light irradiation. *Carbohydr. Polym.* **2016**, *136*, 322–328. [CrossRef] [PubMed]
32. Ai, Z.; Ho, W.; Lee, S. Efficient visible light photocatalytic removal of NO with BiOBr-graphene nanocomposites. *J. Phys. Chem. C* **2011**, *115*, 25330–25337. [CrossRef]
33. Qaiser, A.A.; Hyland, M.M.; Patterson, D.A. Surface and charge transport characterization of polyaniline-cellulose acetate composite membranes. *J. Phys. Chem. B* **2011**, *115*, 1652–1661. [CrossRef] [PubMed]
34. Naeem, H.; Tofil, H.M.; Soliman, M.; Hai, A.; Zaidi, S.H.H.; Kizilbash, N.; Alruwaili, D.; Ajmal, M.; Siddiq, M. Reduced graphene oxide-zinc sulfide nanocomposite decorated with silver nanoparticles for wastewater treatment by adsorption, photocatalysis and antimicrobial action. *Molecules* **2023**, *28*, 926. [CrossRef]
35. Jia, Y.; Liu, P.; Wang, Q.; Wu, Y.; Cao, D.; Qiao, Q.A. Construction of Bi_2S_3-BiOBr nanosheets on TiO_2 NTA as the effective photocatalysts: Pollutant removal, photoelectric conversion and hydrogen generation. *J. Colloid Inter. Sci.* **2021**, *585*, 459–469. [CrossRef]

36. Pan, L.; Yao, L.; Mei, H.; Liu, H.; Jin, Z.; Zhou, S.; Zhang, M.; Zhu, G.; Cheng, L.; Zhang, L. Structurally designable Bi_2S_3/P-doped ZnO S-scheme photothermal metamaterial enhanced CO_2 reduction. *Sep. Purif. Technol.* **2023**, *312*, 123365. [CrossRef]
37. Fang, L.; Zhang, B.; Li, W.; Li, X.; Xin, T.; Zhang, Q. Controllable synthesis of ZnO hierarchical architectures and their photocatalytic property. *Superlattices Microstruct.* **2014**, *75*, 324–333. [CrossRef]
38. Zeng, L.; Zhao, H.; Zhu, Y.; Chen, S.; Zhang, Y.; Wei, D.; Sun, J.; Fan, H. A one-pot synthesis of multifunctional Bi_2S_3 nanoparticles and the construction of core–shell Bi_2S_3@ Ce_6-CeO_2 nanocomposites for NIR-triggered phototherapy. *J. Mater. Chem. B* **2020**, *8*, 4093–4105. [CrossRef]
39. Wang, X.; Lv, R.; Wang, K. Synthesis of ZnO@ZnS-Bi_2S_3 core-shell nanorod grown on reduced graphene oxide sheets and its enhanced photocatalytic performance. *J. Mater. Chem. A* **2014**, *2*, 8304–8313.
40. Xiao, S.; Shen, Z.; Song, S.; Han, S.; Du, Y.; Wang, H. Enhanced sulfadiazine degradation in a multi-electrode paralleling DBD plasma system coupled with ZnO/cellulose acetate films. *J. Environ. Chem. Eng.* **2023**, *11*, 109063. [CrossRef]
41. Wang, Y.; Dai, L.; Qu, K.; Qin, L.; Zhuang, L.; Yang, H.; Xu, Z. Novel Ag-AgBr decorated composite membrane for dye rejection and photodegradation under visible light. *Front. Chem.* **2021**, *15*, 892–901. [CrossRef]
42. Jian, J.; Kuang, D.; Wang, X.; Zhou, H.; Gao, H.; Sun, W.; Yuan, Z.; Zeng, J.; You, K.; Luo, H.A. Highly dispersed Co/SBA-15 mesoporous materials as efficient and stable catalyst for partial oxidation of cyclohexane with molecular oxygen. *Mater. Chem. Phys.* **2020**, *246*, 122814. [CrossRef]
43. Jian, J.; Yang, D.; Liu, P.; You, K.; Sun, W.; Zhou, H.; Yuan, Z.; Ai, Q.; Luo, H. Solvent-free partial oxidation of cyclohexane to KA oil over hydrotalcite-derived Cu-MgAlO mixed metal oxides. *Chin. J. Chem. Eng.* **2022**, *42*, 269–276. [CrossRef]
44. Son, W.K.; Youk, J.H.; Lee, T.S.; Park, W.H. Preparation of antimicrobial ultrafine cellulose acetate fibers with silver nanoparticles. *Macromol. Rapid Commun.* **2004**, *25*, 1632–1637. [CrossRef]
45. El-Sheikh, S.M.; Azzam, A.B.; Geioushy, R.A.; Farida, M.; Salah, B.A. Visible-light-driven 3D hierarchical Bi_2S_3/BiOBr hybrid structure for superior photocatalytic Cr(VI) reduction. *J. Alloys Compd.* **2021**, *857*, 157513. [CrossRef]
46. Jatoi, A.W.; Kim, I.S.; Ni, Q. Cellulose acetate nanofibers embedded with AgNPs anchored TiO_2 nanoparticles for long term excellent antibacterial applications. *Carbohydr. Polym.* **2019**, *207*, 640–649. [CrossRef] [PubMed]
47. Ahmad, I.; Shukrullah, S.; Naz, M.Y.; Bhatti, H.N. Dual S-scheme ZnO-gC_3N_4-CuO heterosystem: A potential photocatalyst for H_2 evolution and wastewater treatment. *React. Chem. Eng.* **2023**, *8*, 1159–1175. [CrossRef]
48. Sivaranjini, B.; Mangaiyarkarasi, R.; Ganesh, V.; Umadevi, S. Vertical alignment of liquid crystals over a functionalized flexible substrate. *Sci. Rep.* **2018**, *8*, 8891. [CrossRef]
49. Xu, T.; Zhang, L.; Cheng, H.; Zhu, Y. Significantly enhanced photocatalytic performance of ZnO via graphene hybridization and the mechanism study. *Appl. Catal. B* **2011**, *101*, 382–387. [CrossRef]
50. Kumar, S.; Sharma, S.; Umar, A.; Kansal, S.K. Bismuth sulphide (Bi_2S_3) nanotubes as an efficient photocatalyst for methylene blue dye degradation. *Nanosci. Nanotechnol. Lett.* **2016**, *8*, 266–272. [CrossRef]
51. Wang, X.; Sui, Y.; Jian, J.; Yuan, Z.; Zeng, J.; Zhang, L.; Wang, T.; Zhou, H. Ag@AgCl nanoparticles in-situ deposited cellulose acetate/silk fibroin composite film for photocatalytic and antibacterial applications. *Cellulose* **2020**, *27*, 7721–7737. [CrossRef]
52. Ji, X.; Li, C.; Liu, J.; Zhang, T.; Yang, Y.; Yu, R.; Luo, X. Controlled Synthesis and Visible-Light-Driven Photocatalytic Activity of BiOBr Particles for Ultrafast Degradation of Pollutants. *Molecules* **2023**, *28*, 5558. [CrossRef]
53. Xu, J.; Jian, J.; Dan, Y.; Song, J.; Meng, L.; Deng, P.; Sun, W.; Zhang, Y.; Xiong, J.; Yuan, Z.; et al. Durable and recyclable BiOBr/silk fibroin-cellulose acetate composite film for efficient photodegradation of dyes under visible light irradiation. *Front. Chem. Sci. Eng.* **2023**, 1–11. [CrossRef]
54. Li, Y.; Sun, X.; Tang, Y.; Ng, Y.H.; Li, L.; Jiang, F.; Wang, J.; Chen, W.; Li, L. Understanding photoelectrocatalytic degradation of tetracycline over three-dimensional coral-like ZnO/$BiVO_4$ nanocomposite. *Mater. Chem. Phys.* **2021**, *271*, 124871. [CrossRef]
55. Murugadoss, G.; Salla, S.; Kumar, M.R.; Kandhasamy, N.; Al Garalleh, H.; Garaleh, M.; Brindhadevi, K.; Pugazhendhi, A. Decoration of ZnO surface with tiny sulfide-based nanoparticles for improve photocatalytic degradation efficiency. *Environ. Res.* **2023**, *220*, 115171. [CrossRef] [PubMed]
56. Zou, M.; Tan, C.; Yang, H.; Kuang, D.; Nie, Z.; Zhou, H. Facile preparation of recyclable and flexible BiOBr@TiO_2/PU-SF composite porous membrane for efficient photocatalytic degradation of mineral flotation wastewater. *J. Water Process Eng.* **2022**, *50*, 103127. [CrossRef]

Disclaimer/Publisher's Note: The statements, opinions and data contained in all publications are solely those of the individual author(s) and contributor(s) and not of MDPI and/or the editor(s). MDPI and/or the editor(s) disclaim responsibility for any injury to people or property resulting from any ideas, methods, instructions or products referred to in the content.